Local amorphization in boron carbide at finite temperature: Strategies toward improved ductility

Jun Li [1], Qi An [2,*] and Lisheng Liu [1]

[1]*State Key Laboratory of Advanced Technology for Materials Synthesis and Processing, Wuhan University of Technology, Wuhan 430070, China*
[2]*Department of Chemical and Materials Engineering, University of Nevada-Reno, Reno, Nevada 89557, USA*

Boron carbide (B_4C) is superhard, but its engineering applications are limited by the abnormal brittle failure arising from amorphous shear band formation. Mitigating the local amorphization is essential to improve the ductility of B_4C. Here, we carried out *ab initio* molecular dynamics (AIMD) simulations to examine the response of B_4C to shear along two plausible slip systems $(001)/[100]$ and $(111)/[11\bar{2}]$ at finite temperature. We found that the icosahedra of B_4C gradually deconstruct at finite temperature, resulting in local amorphization, thereby giving rise to a lower stress barrier than that of density functional theory simulations at zero temperature. The deconstruction of the icosahedral clusters arises from the interaction with the neighboring chains. The failure mechanism at the finite temperature suggested that the local amorphization can be suppressed by altering the structure of the 12-atom icosahedron and the 3-atom chain of B_4C. To demonstrate this, we replaced the $B_{11}C^P$ icosahedron in B_4C with B_{12} icosahedron to form boron-rich boron carbide ($B_{13}C_2$) and then performed the same shear deformations. We found that local amorphization significantly decreases, which results from the modified icosahedral interaction. We also altered the 3-atom C-B-C chain to the 2-atom P-P chain and found that the accumulated shear stress can be released through icosahedral slipping, which is achieved by breaking the chains. The icosahedral slipping then prevents the destruction of icosahedra under shear deformations, expected to improve the ductility. Our results demonstrate two design strategies toward improved ductility of B_4C: (1) boron enrichment can alleviate amorphous shear band formation in boron carbide, and (2) altering the 3-atom chain to a 2-atom chain and meanwhile decreasing the strength of the chain to make it less stable than the icosahedron cage may lead to an icosahedral-slipping-dominated mechanism, thereby avoiding icosahedral fracture.

I. INTRODUCTION

As one of the superhard ceramics, boron carbide (B_4C) exhibits many superior physical properties, such as ultrahigh hardness, low density, high melting temperature, high thermal stability, and extreme wear resistance, making it of practical importance for a wide range of science and engineering applications including abrasives powers, refractories, semiconductors, and ballistic armor [1–3]. However, B_4C softens and fractures easily just above its Hugoniot elastic limit (HEL $\approx$ 20 GPa) under extreme environments of high pressures and hypervelocity impact [4–6], which greatly impedes its extended engineering applications. This abnormal brittle failure of B_4C arises from the formation of amorphous shear bands, which has been identified under various test conditions such as hypervelocity impact [7], indentation [8,9], mechanical scratching [8,10], diamond anvil cell [11], laser shock [12], and radiation [13]. Researchers have attempted to explain the atomistic mechanism underlying amorphous shear band formation in B_4C by both experimental and theoretical studies [14–20]. We carried out quantum mechanics (QM) calculations to examine the response of B_4C to shear along 11 slip systems and discovered that the slip system with the

lowest shear strength $(001)/[100]$ results in a unique deformation mechanism where a B-C bond between neighboring icosahedra breaks to form a carbon lone pair (Lewis base) on the C within the icosahedron [19]. Then further shear leads this Lewis base C to form a new bond with the Lewis acidic B in the middle of a 3-atom CBC chain. This stretches the icosahedra and initiates the destruction of the icosahedra and subsequent failure [19]. Recently, Reddy *et al.* [21] employed depth-sensitive nanoindentation to probe the structural evolution of single-crystal B_4C. The transmission electron microscopy (TEM) characterization suggested that the amorphization of B_4C is mediated by dislocations along some slip systems, rather than a directive crystal-to-amorphous transition. In addition to dislocations, both asymmetric and symmetric twins in B_4C have been observed experimentally, but only symmetric twins in $B_{13}C_2$ [22,23], which may have significant influences on the amorphization of boron carbide. In addition, elastic instability may be another reason for the onset of amorphization in B_4C [24,25]. Grady [24] suggested that the amorphization in B_4C is a consequence of adiabatic shear deformation in the impact event and then predicted the nominal width and spacing of adiabatic shear bands in B_4C using continuum energy principles. Clayton [25] developed a nonlinear constitutive model to examine the mechanical stability of B_4C using several stability criteria, which captures the loss of elastic stability of B_4C with increasing compression.

*Corresponding author: qia@unr.edu

In fact, the formation of amorphous shear bands in B_4C is often accompanied by dramatic changes in pressures and temperatures [12,26,27]. However, only the high pressure was considered in most theoretical studies using QM simulations, while the other important factor, temperature, was often neglected, even though the temperature plays an essential role in explaining the complexities of deformation behaviors [26,27]. Recently, we performed large-scale reactive force field molecular dynamics simulations of shear deformations in B_4C at room temperature and found that brittle failure of B_4C results from the formation of higher density amorphous bands due to fracture of icosahedra, leading to tension-induced cavitation followed by crack opening and failure [15]. Subhash *et al.* [26,27] found that, when subjected to the shock loading, the temperature of the B_4C system could rise rapidly above its melting point even at low impact velocity. Then they discussed the relationship between the pressure-induced temperature rise and shock deformation of B_4C [26,27]. Although the need for studying the connection between temperature and deformation behaviors of B_4C has been emphasized, it is very challenging to develop a good force field for atomistic simulations of B_4C with intriguing bonding characters.

Developing high-strength and high-ductility materials is of great interest for science and engineering applications. To extend the engineering applications of B_4C, it is essential to mitigate its amorphous shear band formation by suppressing the deconstruction of icosahedral clusters under highly compressed conditions. Many approaches have been suggested and examined to improve the ductility of B_4C. For example, previous experimental and theoretical studies demonstrated that doping impurity elements such as Mg [28,29], Li [30,31], and Si [32–34] into B_4C can improve its theoretical strength or mitigate the formation of amorphous shear bands. Multiple-phase material B_4C-B_6O has been proposed to improve the ductility by suppressing the failure mechanism of B_4C [35]. Another approach is to introduce nanoscale twins into B_4C which can significantly improve its intrinsic strength and fracture toughness, thereby mitigating the formation of amorphous shear bands [23,36]. Moreover, injecting electrons into B_4C can both enhance its strength and ductility due to the modified failure mechanism arising from the distribution of excess electrons [37].

B_4C has a unique crystal structure among engineering ceramics, which consists of a 12-atom boron-rich icosahedron ($B_{11}C^P$) located at vertices of a rhombohedral unit cell and a linear 3-atom chain (CBC) along the diagonal axis [38,39], as shown in Fig. S1(a) of the Supplemental Material [40]. Modifying the structure of both the 12-atom icosahedron and the 3-atom chain has been suggested as a promising avenue for mitigating the formation of amorphous shear bands in B_4C [33,41–44]. QM simulations suggested that replacing the C atom with the B atom in the icosahedron can transform it from $B_{11}C^P$ to B_{12}, which may modify the twin formation [23,45] and the icosahedral interaction, thereby improving the mechanical and fracture properties as well as suppressing amorphous shear band formation [41,42]. In other words, boron enrichment can alleviate amorphization in boron carbide, which has also been validated by experimental studies [46]. The formation of amorphous shear bands may also be suppressed by altering the chain structure from the 3-atom

C-B-C chain to a 2-atom chain [33,34,47,48]. Particularly, replacing the 3-atom C-B-C chain with the 2-atom Si-Si chain, denoted as $B_{11}C^P$-SiSi, can dramatically increase the ductility of boron carbide because the 2-atom Si-Si chain enables the icosahedra to accommodate additional shear by rotation instead of breaking bonds [33]. In addition, our density functional theory (DFT) studies on boron suboxide (B_6O) and boron subphosphide ($B_{12}P_2$) indicate that their icosahedral clusters do not deconstruct shearing along the most favorable slip system at $T = 0$ K [47,48], which also support the idea that altering the 3-atom C-B-C chain to a 2-atom chain can be considered as a potential avenue for improving ductility.

Here, we carried out an *ab initio* molecular dynamics (AIMD) method to apply pure shear deformations on B_4C along two plausible slip systems at finite temperature: (i) $(001)/[100]$ (the hexagonal representation is $(01\bar{1}\bar{1})/[\bar{1}101]$), which is related to amorphous shear band formation [9,19], and (ii) $(111)/[11\bar{2}]$ (the hexagonal representation is $(0001)/[10\bar{1}0]$), which is related to deformation twinning [15,49]. The deformation behaviors and failure mechanism of B_4C at finite temperature have been examined and compared with that of B_4C under the adiabatic condition ($T = 0$ K). Note that the adiabatic condition in QM refers to a physical system remaining in its instantaneous eigenstate if a given perturbation is acting on it slowly enough and if there is a gap between the eigenvalue and the rest of the Hamiltonian's spectrum [50]. The deformation processes suggest that, instead of fully disintegrated simultaneously at $T = 0$ K, the icosahedra in B_4C are gradually deconstructed, forming local amorphization at finite temperature. The investigation of the shear performance of B_4C at finite temperature provides insight into understanding the amorphous shear band formation in boron carbide.

Next, we report the investigations of the pure shear deformations of $B_{13}C_2$ and $B_{12}P_2$ along the two slip systems of $(001)/[100]$ and $(111)/[11\bar{2}]$ at finite temperature to illustrate the design strategies for improved ductility. Our results show that boron enrichment may lead to local structural failure where some icosahedra remain intact instead of full destruction in which all icosahedra are disintegrated, thereby mitigating amorphous shear band formation. Replacing the 3-atom chain with a 2-atom chain is a promising way for modifying the deformation mechanism to icosahedral slipping without fracturing icosahedra so that the ductility can be enhanced. We consider that these results on the deformation mechanisms of $B_{13}C_2$ and $B_{12}P_2$ at finite temperature can provide hints on enhancing the ductility of boron carbide.

II. METHODS

All simulations were performed using the Vienna *ab initio* Simulation Package (VASP) periodic code with plane-wave basis set [51–53], employing the Perdew-Burke-Ernzerhof functional form of the generalized gradient approximation for describing the exchange and correlation energy of electrons [54]. The plane-wave projector augmented wave method was adopted to generate the pseudopotential, representing the interaction between cores and valence electrons [55]. The plane-wave cutoff energy was determined to be 500 eV in all simulations, which could provide excellent convergence

on energy, force, stress, and geometry. The energy convergence for electronic self-consistent field (SCF) interaction and the force convergence for the ion relaxation were set to 1×10^{-6} eV and 5×10^{-3} eV/Å, respectively. The Brillouin-zone integration was performed on Γ-centered symmetry-reduced Monkhorst-Pack meshes with a fine resolution of $< 2\pi \times \frac{1}{60}$ Å^{-1} except for the shear simulations.

We performed the AIMD simulations to examine the pure shear deformation behaviors of B_4C, $B_{13}C_2$, and $B_{12}P_2$ at finite temperature. We first constructed the supercell of these systems and then optimized the cell parameters and atomic positions using DFT at $T = 0$ K. Next, they were equilibrated at room temperature using constant pressure, constant temperature, and constant number of atoms (NPT ensemble), where the temperature and pressure were controlled by the Langevin thermostat and Parinello-Rahman barostat, respectively. Finally, we applied pure shear strain on these systems with an increment shear strain of 0.02. In each shear strain, these systems were equilibrated at the finite temperature ($T = 300$ K) for 3 ps using constant volume, constant temperature, and constant number of atoms (NVT ensemble), leading to a strain rate of 6.67×10^9 s^{-1}. The temperature was also controlled by the Langevin thermostat. A time step of 1.0 fs was adopted for integrating the equation of motion. The periodic boundary conditions were applied to minimize the plausible surface effects. The energy error for terminating electronic SCF was set to 1×10^{-4} eV, and the force criterion for atom relaxation was set to 1×10^{-2} eV/Å in the AIMD simulations.

To determine the failure mechanism under finite shear deformation, we applied the pure shear strain on a particular shear plane. At each deformation step, a shear strain was applied sequentially to the structure relaxed in the previous step for achieving imposing continuously shear deformations. For the shear simulations, we used supercells varying from 84 to 120 atoms of three superhard materials along two plausible slip systems while only the Γ point was sampled in the Brillouin zone. The stress-strain relationships were computed to explain the mechanical behaviors as well as to identify the failure modes. In addition, the electron localization function (ELF) analysis, whose values range from 0 to 1, was performed to analyze the bond broken and reformation, as well as the long pair formation during the shear deformation process [56–58]. The VESTA software [58] was employed to visualize the crystal structures and ELF. It should be noted that the structural evolution during shear deformation is visualized by rotating the a axis along the x direction in this paper.

III. RESULTS AND DISCUSSION

A. Deformation and failure mechanism of B_4C at finite temperature

The crystalline structures of B_4C, $B_{13}C_2$, and $B_{12}P_2$ are like that of the α-rhombohedral phase of boron (space group $R\bar{3}m$), as shown in Figs. S1(a), S2(a), and S3(a) of the Supplemental Material [40], respectively. They are composed of one icosahedron located at vertices of a rhombohedral unit cell plus a linear chain having two to three atoms along the diagonal axis that interconnects the icosahedra. The structural configurations of B_4C, $B_{13}C_2$, and $B_{12}P_2$ can be represented

as $B_{11}C^P$-CBC, B_{12}-CBC, and B_{12}-PP, where the C^P atom is in the polar site of the icosahedron. Since the substitution of the C atom into the B_{12} icosahedron induces small distortions in the $R\bar{3}m$ symmetry [15], the optimized equilibrium lattice parameters of B_4C are given as $a = 5.207$ Å, $b = 5.057$ Å, $c = 5.207$ Å, $\alpha = 66.012°$, $\beta = 65.159°$, and $\gamma = 66.012°$, leading to a density of $\rho = 2.525$ g/cm^3, which are consistent with experimental values of $a = 5.171$ Å, $\alpha = 65.68°$, and $\rho = 2.518$ g/cm^3 [3]. The calculated lattice parameters for $B_{13}C_2$ and $B_{12}P_2$ are $a = 5.171$ Å, $\alpha = 65.68°$, and $a = 5.171$ Å, $\alpha = 65.68°$, respectively, which are in good agreement with previous calculations and experimental data [39,47,59].

To illustrate the failure mechanism of B_4C at finite temperature, we examined the shear deformation behaviors of B_4C along two plausible slip systems (001)/[100] and (111)/[11$\bar{2}$] at $T = 300$ K and compared them with those at $T = 0$ K. Figure S1(b) of the Supplemental Material [40] shows the shear simulation model of B_4C along the (001)/[100] slip system expected to be favorable for the formation of amorphous shear bands, where the B-C bond between neighboring icosahedra is stretched under shear deformations. Figure 1(a) displays the shear-stress-shear-strain relationships of B_4C along the (001)/[100] slip system at both $T = 0$ and 300 K. At $T = 0$ K, the shear stress initially increases almost linearly up to the maximum value of 46.04 GPa as the shear strain increases to $\varepsilon = 0.227$, indicating that the B_4C structure is uniformly resistant to the elastic deformation. Then the shear stress decreases slightly to 43.19 GPa at $\varepsilon = 0.245$ and suddenly drops to 27.80 GPa at $\varepsilon = 0.297$, indicating a dramatic structural change. On further shear deformation, the shear stress ultimately drops to the minimum value of 10.11 GPa at $\varepsilon = 0.331$. At the finite temperature ($T = 300$ K), the shear stress first increases monotonically to the maximum value of 42.44 GPa at $\varepsilon = 0.209$. The critical shear stress of B_4C at $T = 300$ K is 7.8% lower than that at $T = 0$ K (46.04 GPa), suggesting that the temperature leads to a lower stress barrier of forming amorphous shear bands in B_4C. Beyond the point of maximum shear stress, there is a dramatic drop in shear stress to 27.82 GPa at $\varepsilon = 0.227$. After the shear stress decreases to 16.95 GPa at $\varepsilon = 0.245$, it fluctuates with increasing shear strain, implying the structural failure. As shown in Fig. 1(a), the shear-stress-shear-strain relationship of B_4C at $T = 0$ K exhibits different behaviors from that of the finite temperature, when the shear strain increases above $\varepsilon = 0.20$. To determine whether the deformed B_4C structure is metastable or not at $T = 0$ K, we performed AIMD simulations at $\varepsilon = 0.227$. The results show that B_4C keeps the original structure after 3 ps of MD run, suggesting it is intrinsically metastable. Thus, the difference of the room temperature shear-stress-shear-strain curve at large strain from that of $T = 0$ K is due to the temperature effect instead of the dynamical instability.

Figures 1(b)–1(f) and 2(a)–2(d) show the structures and the isoelectron surface (at 0.85) from the ELF analysis at various critical strains at $T = 0$ and 300 K, respectively, along the (001)/[100] slip system. Figure 1(b) shows the intact structure. As the shear strain increases to $\varepsilon = 0.227$, corresponding to the maximum shear stress, the distance of the B-C bond between neighboring icosahedra increases by 23% to 2.043 Å,

(a) the shear-stress-shear-strain relationships

(b) ε = 0.0

(c) ε = 0.227

(d) ε = 0.245
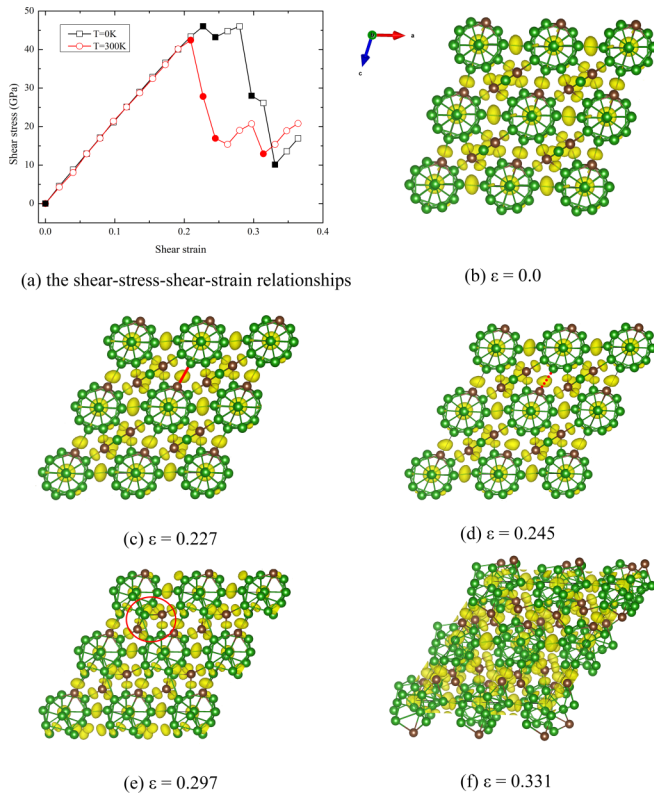
(e) ε = 0.297

(f) ε = 0.331

FIG. 1. The shear-stress-shear-strain relationships, calculated isosurfaces (at 0.85) of the electron localization function (ELF) and the structural evolution of B_4C shearing along the $(001)/[100]$ slip system at $T = 0$ K. (a) the shear-stress-shear-strain relationships. (b) The initial structure. (c) The structure at $\varepsilon = 0.227$ corresponding to the maximum shear stress, where the B-C bond between icosahedra is stretched. (d) The structure at $\varepsilon = 0.245$, where the B-C bond between icosahedra is broken. (e) The structure at $\varepsilon = 0.297$ after the first stress drop, where the sudden bending of the 3-atom chain occurs that initiates the destruction of icosahedra. (f) The structure at $\varepsilon = 0.331$, where the icosahedra are fully deconstructed simultaneously, resulting in structural failure. The boron and carbon atoms are represented by the green and sienna balls, respectively.

as shown in Fig. 1(c). Continuous shearing to $\varepsilon = 0.245$ leads to a small stress decrease arising from the breaking of the B-C bond between icosahedra because the distance of the B-C bond increases to 2.227 Å, and its ELF moves totally to the icosahedral carbon, as displayed in Fig. 1(d). As the shear strain increases to $\varepsilon = 0.297$ [Fig. 1(e)], the sudden bending of the 3-atom chain occurs, forming new B-B bonds between neighboring icosahedra and chains. This then initiates the destruction of icosahedra. Finally, continuous shear totally disintegrates the icosahedral clusters simultaneously, leading to amorphization, thereby resulting in structural failure, as displayed in Fig. 1(f).

To characterize the amorphization in B_4C, we then calculated the radial distribution function (RDF) to distinguish the crystal and amorphous phases. As shown in Fig. S4 of the Supplemental Material [40], the RDF plot of undeformed B_4C structure has well-defined peak features and displays long-range order which is associated with the crystal structure. The well-defined peaks correspond to different B-C, B-B, and C-C
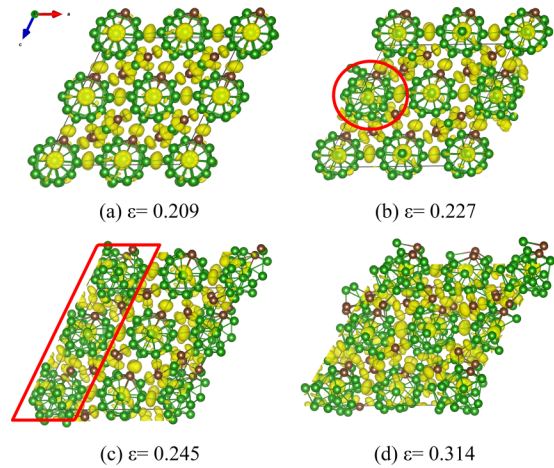

(a) ε= 0.209

(b) ε= 0.227

(c) ε= 0.245

(d) ε= 0.314

FIG. 2. Calculated isosurfaces (at 0.85) of the electron localization function (ELF) and the structural evolution of B_4C shearing along the $(001)/[100]$ slip system at $T = 300$ K. (a) The structure at $\varepsilon = 0.209$ corresponding to the maximum shear stress, where no bond breaks nor forms. (b) The structure at $\varepsilon = 0.227$, where one of the icosahedra is deconstructed. (c) The structure at $\varepsilon = 0.245$, where one layer of icosahedra is disintegrated. (d) The structure at $\varepsilon = 0.314$, where all icosahedra are deconstructed, causing structural failure. The boron and carbon atoms are represented by the green and sienna balls, respectively.

separations. As the shear strain increases to $\varepsilon = 0.331$, the B_4C structure is deconstructed. The distinctive sharp peaks in the RDF disappear, indicating the formation of the amorphous phase. It is worth noting that this failure mechanism is different from the ideal shear deformation [19], where the C-B-C chain reacts with the carbene formed by breaking the icosahedral B-C bond. Instead, the middle B atom in the C-B-C chain interacts with the B atom in the cage, leading to the failure. This suggests that the mechanical loading mode significantly influences the deformation and failure mechanism of B_4C.

The details of deformation processes for B_4C shearing along the $(001)/[100]$ slip system at the finite temperature ($T = 300$ K) are displayed in Figs. 2(a)–2(d). As the shear strain increases, the B_4C system deforms elastically, causing the shear stress to increase continuously until reaching the maximum value of 42.44 GPa at $\varepsilon = 0.209$. No bond breaks nor forms in the process, as shown in Fig. 2(a). With further shear to $\varepsilon = 0.227$, one of the icosahedra is deconstructed, which initiates the amorphization of B_4C [Fig. 2(b)]. At $\varepsilon = 0.245$, one layer of $B_{11}C^P$ icosahedral clusters is disintegrated, forming an amorphous shear band [Fig. 2(c)]. As the shear strain further increases continuously, the shear stress monotonically increases to 20.70 GPa without totally fracturing icosahedra. At critical failure strain $\varepsilon = 0.314$, all icosahedra are totally disintegrated, causing structural failure, as displayed in Fig. 2(d). Therefore, the structural failure of B_4C at finite temperature initiates very locally from deconstructing one icosahedron, and then this cage deconstruction propagates to form one layer of amorphous region.

Next, we examine the shear deformation of B_4C along the $(111)/[11\bar{2}]$ slip system expected to be favorable for the formation of twins along the (111) plane, where the 3-atom C-B-C chains are perpendicular to the slip direction (Fig. S1(c)

(a) the shear-stress-shear-strain relationships

(b) ε = 0.0

(c) ε = 0.209

(d) ε = 0.539

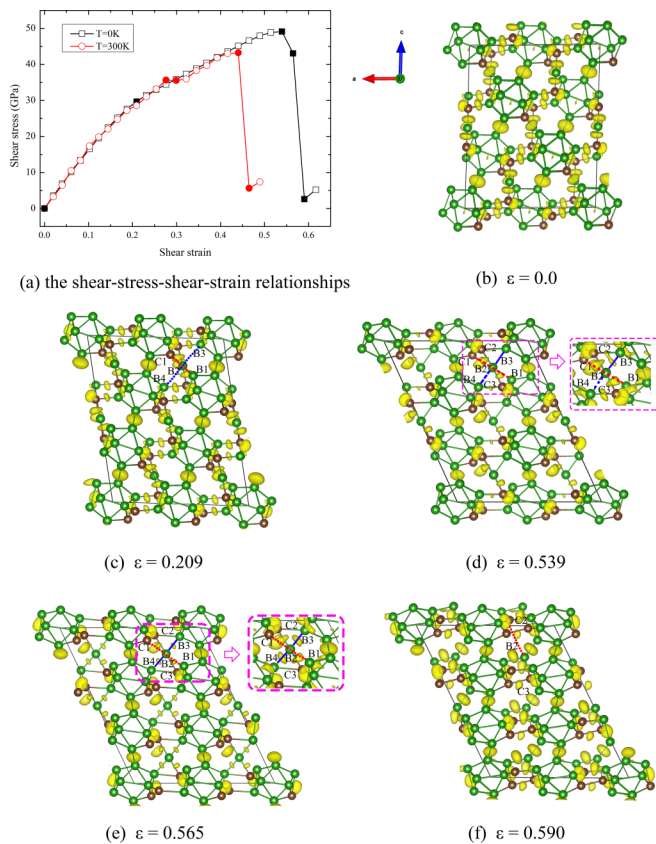
(e) ε = 0.565

(f) ε = 0.590

FIG. 3. The shear-stress-shear-strain relationships, calculated isosurfaces (at 0.85) of the electron localization function (ELF) and the structural evolution of B_4C shearing along the $(111)/[11\bar{2}]$ slip system at $T = 0$ K. (a) The shear-stress-shear-strain relationships. (b) The initial structure. (c) The structure at $\varepsilon = 0.209$, where the B1-C1 bond between icosahedra is broken causing a slope change in the shear-stress-shear-strain curve. (d) The structure at $\varepsilon = 0.539$ corresponding to the maximum shear stress, where a new $3c-2e$ C2-B2-B3 bond forms; the isosurface of the ELF shown in the zoom apart is at 0.8. (e) The structure at $\varepsilon = 0.565$, where new $2c-2e$ B2-B3 and B2-B4 bonds form; the isosurface of the ELF shown in the zoom apart is at 0.8. (f) The structure at $\varepsilon = 0.590$, where the 3-atom chain is broken without fracturing icosahedra. The boron and carbon atoms are represented by the green and sienna balls, respectively.

(a) ε = 0.276

(b) ε = 0.299

(c) ε = 0.440

(d) ε = 0.465

FIG. 4. Calculated isosurfaces (at 0.85) of the electron localization function (ELF) and the structural evolution of B_4C shearing along the $(111)/[11\bar{2}]$ slip system at $T = 300$ K. (a) The structure at $\varepsilon = 0.276$ corresponding to the maximum shear stress, where the B1-C1 bond between icosahedra is stretched. (b) The structure at $\varepsilon = 0.299$, where the B1-C1 bond between icosahedra is broken. (c) The structure at $\varepsilon = 0.440$, where a new $3c-2e$ C2-B2-B3 bond forms; the isosurface of the ELF shown in the zoom apart is at 0.8. (d) The structure at $\varepsilon = 0.465$, where the C5-B5 bond in the 3-atom chain is broken, causing the neighboring icosahedron to fracture followed by the structural failure. The boron and carbon atoms are represented by the green and sienna balls, respectively.

of the Supplemental Material [40]). The shear-stress-shear-strain relationships at both $T = 0$ and 300 K are displayed in Fig. 3(a). Here, the shear strength of B_4C at $T = 300$ K (43.23 GPa) is 12% lower than that at $T = 0$ K (49.15 GPa), implying a lower stress barrier of structural failure in B_4C at finite temperature. The structures and the isoelectron surfaces (at 0.85) from the ELF analysis at various critical strains are displayed in Figs. 3(b)–3(f) to illustrate the failure mechanism shearing along the $(111)/[11\bar{2}]$ slip system at $T = 0$ K. As the intact structure [Fig. 3(b)] is sheared along the $(111)/[11\bar{2}]$ slip system, the B-C bond (B1-C1) between icosahedra is stretched, while the distances between the middle B atom (B2) in the 3-atom chain and the B atoms (B3, B4) in neighboring icosahedra decrease, leading to an almost linear increase in shear stress [Fig. 3(a)]. As shown in Fig. 3(c), when the shear
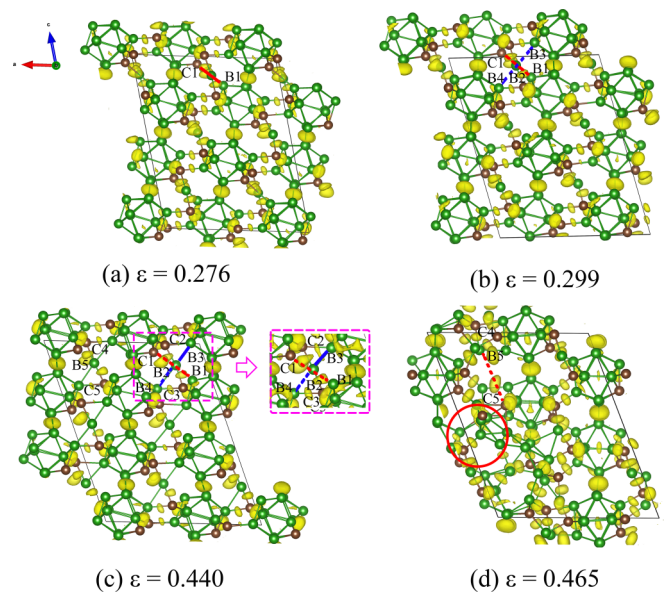
strain increases to $\varepsilon = 0.209$, the ELF of the B1-C1 bond between icosahedra moves totally to the icosahedral carbon, indicating that the B1-C1 bond is broken, thereby causing a slope change in the shear-stress-shear-strain curve [Fig. 3(a)]. Thus, the shear-stress-shear-strain curve exhibits nonlinear behaviors before the shear stress reaches its maximum value. As the shear strain increases to $\varepsilon = 0.539$, corresponding to the maximum shear stress of 49.15 GPa, the C2 chain atom, the B2 chain atom, and the icosahedron B3 atom form a new three-center–two-electron ($3c$-$2e$) bond, as displayed in the zoom part of Fig. 3(d). At $\varepsilon = 0.565$, the ELF in Fig. 3(e) shows the B2 chain atom forms a new bond with the B3 and B4 atoms in the neighboring icosahedra, which is considered as the two-center–two-electron ($2c$-$2e$) bond, leading to the broken C2-B2 chain bond [Fig. 3(f)], relieving the shear stress to 2.59 GPa at $\varepsilon = 0.590$ [Fig. 3(a)]. This failure process suggests that brittle failure of B_4C shearing along the $(111)/[11\bar{2}]$ slip system arises from the deconstruction of 3-atom chains without disintegrating icosahedra, which may explain the formation of the (111) type of twin in B_4C during hot-pressed synthesis processes [7,49].

At $T = 300$ K, the fracture mode of B_4C shearing along the $(111)/[11\bar{2}]$ slip system displays a character like that at $T = 0$ K, as shown in Figs. 4(a)–4(d). As the shear strain increases to $\varepsilon = 0.276$, the B_4C system is uniformly resistant to the elastic deformation, where the B-C bond (B1-C1) between icosahedra is stretched yet not breaking, as shown in Fig. 4(a).

At $\varepsilon = 0.299$, since the ELF of the B1-C1 bond moves totally to the icosahedral carbon [Fig. 4(b)], the B1-C1 bond between icosahedra is broken, causing a slight decrease in shear stress from 35.66 to 35.54 GPa. Meanwhile, the distances between the B atom (B2) in the 3-atom chain and B atoms (B3, B4) in neighboring icosahedra decrease, but the new B-B bond has not been formed yet. With further shear to $\varepsilon = 0.440$, corresponding to the maximum shear stress of 43.23 GPa, there is a new $3c-2e$ C2-B2-B3 bond formation, which is displayed in the zoom part of Fig. 4(c). Finally, the C5-B5 bond in the 3-atom chain is broken [Fig. 4(d)], leading the neighboring icosahedron to fracture while relieving the shear stress to 5.62 GPa at $\varepsilon = 0.465$. However, most icosahedra are still identifiable in this process. This failure process indicates that, at finite temperature, the icosahedron is deconstructed, which arises from the interaction with the neighboring broken chain, causing local structural failure.

The finite-temperature deformation mode of B_4C suggests that the icosahedra in B_4C are gradually deconstructed at finite temperature, which is significantly different from that of B_4C at $T = 0$ K, where all icosahedra are disintegrated simultaneously. This then leads to local amorphization in B_4C, thereby giving rise to a lower stress barrier of amorphous shear band formation in B_4C at finite temperature.

B. Improved ductility of B_4C through boron enrichment

Previous experimental and theoretical studies demonstrated that the formation of amorphous shear bands in B_4C may be mitigated by boron enrichment [41,42,46]. Thus, in this paper, we examine the underlying mechanism by simulating the shear deformation of boron-rich boron carbide ($B_{13}C_2$), which is formed by substituting the $B_{11}C^P$ icosahedron with the B_{12} icosahedron. The same slip systems $(001)/[100]$ and $(111)/[11\bar{2}]$ are considered.

Figure S2(b) of the Supplemental Material [40] displays the shear simulation model of $B_{13}C_2$ shearing along the $(001)/[100]$ slip system, where the B-B bond between neighboring icosahedra is stretched under the shear deformation. The shear-stress-shear-strain relationships of $B_{13}C_2$ at both $T = 0$ and 300 K are shown in Fig. 5(a). The critical shear stress for $B_{13}C_2$ at $T = 300$ K is 30.57 GPa, which is much less than that at $T = 0$ K (43.95 GPa), implying a lower stress barrier of structural failure at finite temperature. To examine how the structure changes of $B_{13}C_2$ under shear deformation, Figs. 5(b)–5(f) and 6(a)–6(d) show the structures and the iso-electron surface (at 0.85) from ELF analysis at various critical strains at $T = 0$ and 300 K, respectively. Figure 5(b) shows the initial structure of $B_{13}C_2$ before shear deformations. As the shear strain increases, the B-B bond between icosahedra stretches continuously, as shown in Figs. 5(c) and 5(d). The ELF analysis indicates that the B-B bond between icosahedra becomes significantly weaker but still exists at $\varepsilon = 0.380$ [Fig. 5(d)], leading to a slight loss of shear stress to 40.44 GPa from the maximum value of 43.95 GPa at $\varepsilon = 0.348$. With further shear to $\varepsilon = 0.397$, there is a sudden bending of the 3-atom chain, causing the formation of new B-B bonds between neighboring icosahedra and chains, as shown in Fig. 5(e). Then the icosahedra start to fracture, and the shear stress gradually drops until reaching its minimum value of 10.79 GPa at

(a) the shear-stress-shear-strain relationships

(b) ε = 0.0

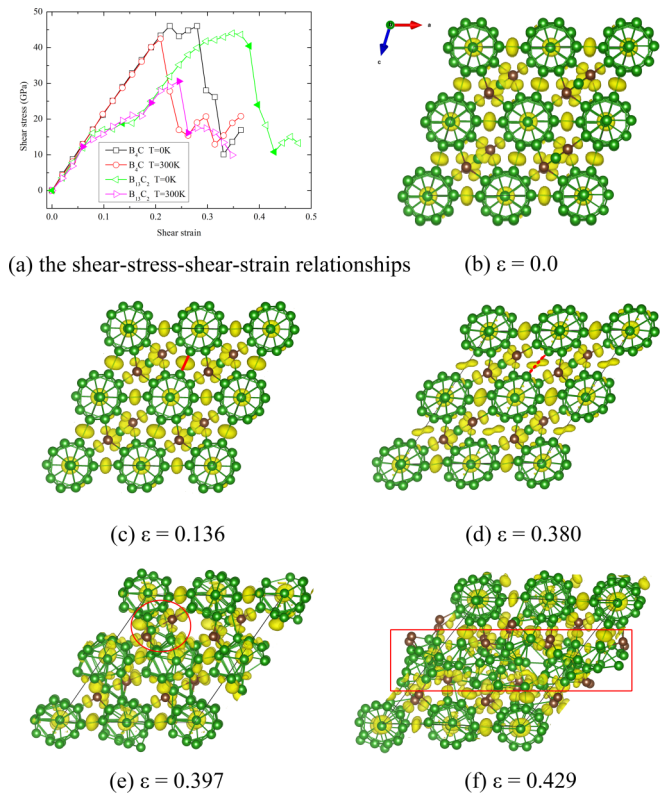(c) ε = 0.136

(d) ε = 0.380

(e) ε = 0.397

(f) ε = 0.429

FIG. 5. The shear-stress-shear-strain relationships, calculated isosurfaces (at 0.85) of the electron localization function (ELF) and the structural evolution of $B_{13}C_2$ shearing along the $(001)/[100]$ slip system at $T = 0$ K. (a) The shear-stress-shear-strain relationships. (b) The initial structure. (c) The structure at $\varepsilon = 0.136$, where the B-B bond between icosahedra is stretched. (d) The structure at $\varepsilon = 0.380$, where the B-B bond between icosahedra becomes significantly weaker but still exists. (e) The structure at $\varepsilon = 0.397$, where the sudden bending of the 3-atom chain occurs that initiates the destruction of icosahedra. (f) The structure at $\varepsilon = 0.429$, where one layer of the icosahedra is deconstructed. The boron and carbon atoms are represented by the green and sienna balls, respectively.

$\varepsilon = 0.429$. Finally, one layer of B_{12} icosahedra in $B_{13}C_2$ is disintegrated [Fig. 5(f)], which is different from that of B_4C, where all icosahedra are totally destroyed simultaneously [Fig. 1(f)]. The failure process suggests less amorphization as the increase of boron content.

The detailed deformation processes of $B_{13}C_2$ shearing along the $(001)/[100]$ slip system at $T = 300$ K are shown in Figs. 6(a)–6(d). As shown in Fig. 6(a), the $B_{13}C_2$ system deforms elastically as the shear strain increases to $\varepsilon = 0.079$. Then continuous shear leads to the bending of the 3-atom chain with random orientations, as displayed in Figs. 6(b) and 6(c). After passing the critical strain, one layer of icosahedra deconstructs at $\varepsilon = 0.262$ [Fig. 6(d)], leading to the fracture failure of $B_{13}C_2$, thereby causing the shear stress to drop from the maximum value of 30.57 to 16.11 GPa.

Next, we investigated the shear deformation of $B_{13}C_2$ along the $(111)/[11\bar{2}]$ slip system, where the 3-atom C-B-C chains are perpendicular to the slip direction, as displayed in Fig. S2(c) of the Supplemental Material [40]. Figure 7(a) shows the shear-stress-shear-strain relationships of $B_{13}C_2$ at

(a) $\varepsilon = 0.079$

(b) $\varepsilon = 0.191$
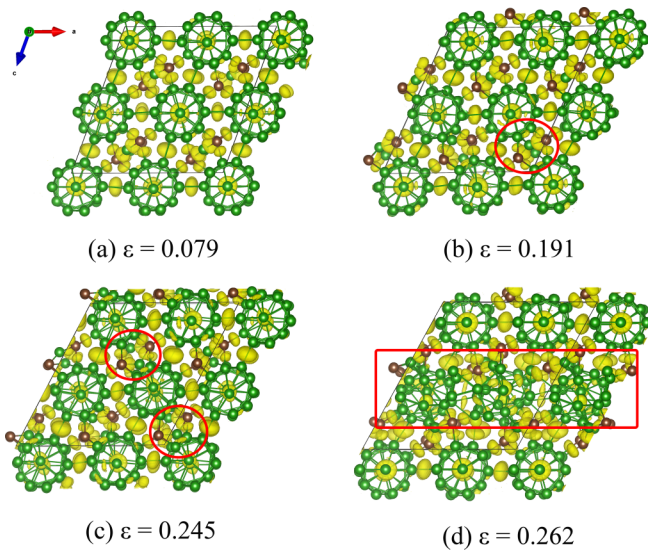
(c) $\varepsilon = 0.245$

(d) $\varepsilon = 0.262$

FIG. 6. Calculated isosurfaces (at 0.85) of the electron localization function (ELF) and the structural evolution of $B_{13}C_2$ shearing along the (001)/[100] slip system at $T = 300$ K. (a) The structure at $\varepsilon = 0.079$, where the system deforms elastically. (b) The structure at $\varepsilon = 0.191$, where some 3-atom chains are bending. (c) The structure at $\varepsilon = 0.245$ corresponding to the maximum shear stress, where all 3-atom chains are bending with random orientations. (d) The structure at $\varepsilon = 0.262$, where one layer of the icosahedra is deconstructed. The boron and carbon atoms are represented by the green and sienna balls, respectively.

(a) the shear-stress-shear-strain relationships

(b) $\varepsilon = 0.0$

(c) $\varepsilon = 0.369$

(d) $\varepsilon = 0.392$
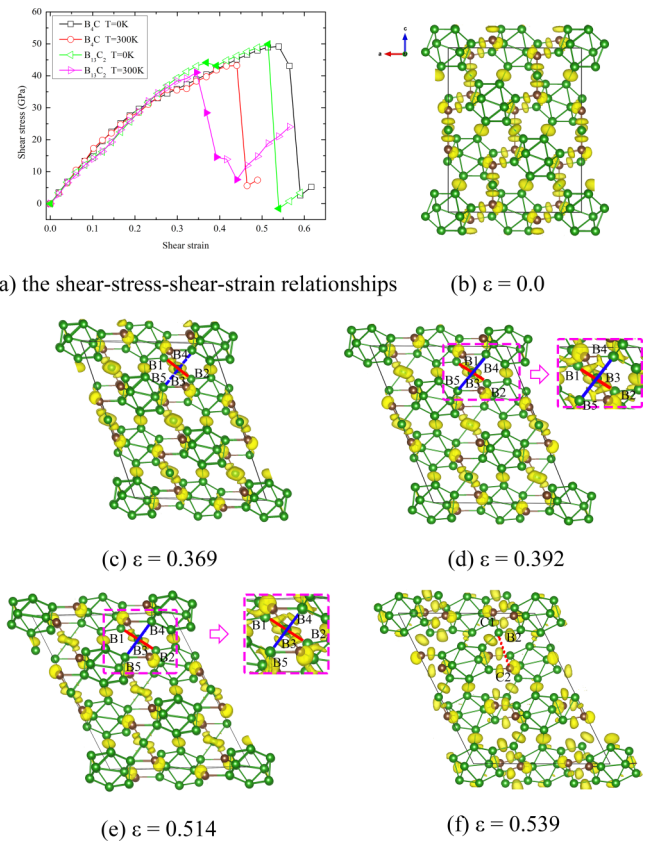
(e) $\varepsilon = 0.514$

(f) $\varepsilon = 0.539$

FIG. 7. The shear-stress-shear-strain relationships, calculated isosurfaces (at 0.85) of the electron localization function (ELF) and the structural evolution of $B_{13}C_2$ shearing along the (111)/[11$\bar{2}$] slip system at $T = 0$ K. (a) The shear-stress-shear-strain relationships. (b) The initial structure. (c) The structure at $\varepsilon = 0.369$, where the B-B bond between icosahedra is stretched and the interaction between chain B3 atom and icosahedra B4 and B5 atoms is enhanced. (d) The structure at $\varepsilon = 0.392$, where new weak B3-B4 and B3-B5 bonds between the 3-atom chain and icosahedra are formed; the isosurface of the ELF shown in the zoom apart is at 0.8. (e) The structure at $\varepsilon = 0.514$, where the B3-B4 and B3-B5 bonds become stronger; the isosurface of the ELF shown in the zoom apart is at 0.8. (f) The structure at $\varepsilon = 0.539$, where the 3-atom chain is deconstructed. The boron and carbon atoms are represented by the green and sienna balls, respectively.

both $T = 0$ and 300 K. The stress barrier of $B_{13}C_2$ at $T = 300$ K is 41.04 GPa, which is 18% lower than that at $T = 0$ K (49.89 GPa). The detailed deformation processes of $B_{13}C_2$ shearing along the (111)/[11$\bar{2}$] slip system at $T = 0$ K are displayed in Figs. 7(b)–7(f). As the intact structure [Fig. 7(b)] is sheared, the B-B bond (B1-B2) between icosahedra is stretched. Different from breaking the icosahedral B-C bond in B_4C, the ELF analysis shows that, although the icosahedral B-B bond in $B_{13}C_2$ becomes significantly weaker, it is not broken before the structural failure, as displayed in Figs. 7(c)–7(e). As the shear strain increases to $\varepsilon = 0.369$, the interaction between the chain B atom (B3) and B atoms (B4, B5) in neighboring icosahedra is enhanced, due to the decreased distance, as displayed in Fig. 7(c). With further shear to $\varepsilon = 0.392$, the chain B3 atom is bonded to icosahedral B4 and B5 atoms, forming new weak B3-B4 and B3-B5 bonds between the 3-atom chain and the neighboring icosahedra, as shown in the zoom part of Fig. 7(d). This leads to a slight decrease in shear stress from 44.13 to 43.14 GPa, as shown in Fig. 7(a). Then as the shear strain increases to $\varepsilon = 0.514$, the B3-B4 and B3-B5 bonds become stronger due to the decreased distance [Fig. 7(e)], leading to the continuous increase of the shear stress until reaching its maximum value of 49.89 GPa. Finally, continuous shear breaks the C2-B2 bond, destroying the 3-atom chain without fracturing icosahedra [Fig. 7(f)], thereby giving rise to a dramatic drop in shear stress to a negative value of −1.50 GPa.

Figures 8(a)–8(d) display the detailed deformation process of $B_{13}C_2$ shearing along the (111)/[11$\bar{2}$] slip system at $T = 300$ K. As the shear strain increases to $\varepsilon = 0.345$, the

$B_{13}C_2$ system undergoes elastic deformations, and its shear stress reaches the maximum value of 41.04 GPa [Fig. 7(a)], where no bond breaks nor forms in the process, as shown in Fig. 8(a). With further shear to $\varepsilon = 0.369$, there are dramatic changes in some 3-atom chains, leading to the first shear stress drop. As displayed in Fig. 8(b), the C1-B1 bond in the 3-atom C1-B1-C2 chain is broken. Meanwhile, the bending of the 3-atom C3-B2-C4 chain occurs, leading to the formation of a new B2-B3 bond between the chain and the icosahedron, thereby causing a gradually and dramatically drop in shear stress [Fig. 7(a)]. These deformations of 3-atom chains then initiate the destruction of icosahedra, as shown in Fig. 8(c). However, it is interesting that, as the shear strain continuously increases to $\varepsilon = 0.440$, some deconstructed 3-atom chains and icosahedra can be self-healed, leading to the local

(a) ε = 0.345
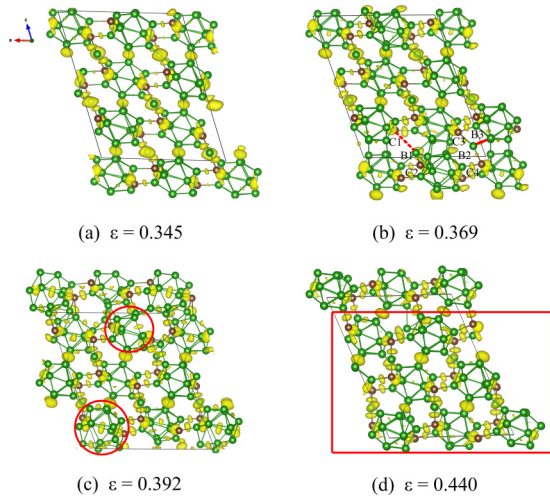
(b) ε = 0.369

(c) ε = 0.392

(d) ε = 0.440

FIG. 8. Calculated isosurfaces (at 0.85) of the electron localization function (ELF) and the structural evolution of $B_{13}C_2$ shearing along the $(111)/[11\bar{2}]$ slip system at $T = 300$ K. (a) The structure at $\varepsilon = 0.345$, where $B_{13}C_2$ deforms elastically. (b) The structure at $\varepsilon = 0.369$, where some 3-atom chains are broken. (c) The structure at $\varepsilon = 0.392$, where some icosahedra are deconstructed. (d) The structure at $\varepsilon = 0.440$, where the $B_{13}C_2$ structure local recovers. The boron and carbon atoms are represented by the green and sienna balls, respectively.

recovery of the structure, as shown in Fig. 8(d). The local recovery of $B_{13}C_2$ demonstrated the excellent capability of the icosahedral cluster at finite temperature and may be very useful for improving the ductility of superhard icosahedral solids.

The deformation mode of $B_{13}C_2$ indicates that the failure mechanism of $B_{13}C_2$ does not involve the B-B bond breaking between icosahedra, which differs from that of B_4C, where the B-C bond between icosahedra is stretched and broken to form a reactive carbene. This may explain why the twins play quite different roles in the B_4C and $B_{13}C_2$ structures [36,46]. The modified icosahedral interaction may improve the ductility by favoring local destruction in $B_{13}C_2$ instead of fully deconstructed where all icosahedra are disintegrated. Thus, variations in stoichiometry, particularly boron enrichment, offer a potential path for improving the ductility of boron carbide and its shock performance.

C. Improved ductility of B_4C through replacing the 3-atom chain with a 2-atom chain

The amorphization of B_4C may also be suppressed by replacing the 3-atom chain with a 2-atom chain [33,34,47,48]. Here, we examine the shear deformation of $B_{12}P_2$ to illustrate this design strategy for improved ductility. Figure S3(b) of the Supplemental Material [40] shows the shear simulation model of $B_{12}P_2$ along the $(001)/[100]$ slip system. The shear-stress-shear-strain relationships of $B_{12}P_2$ shearing along the $(001)/[100]$ slip system at both $T = 0$ and 300 K are shown in Fig. 9(a). The critical shear stress for $B_{12}P_2$ at $T = 300$ K is 40.38 GPa, which is slightly less than the value of 43.20 GPa at $T = 0$ K, suggesting that the stress barrier of structural failure in $B_{12}P_2$ decreases at finite temperature. To explain

(a) the shear-stress-shear-strain relationships

(b) ε = 0.0

(c) ε = 0.262
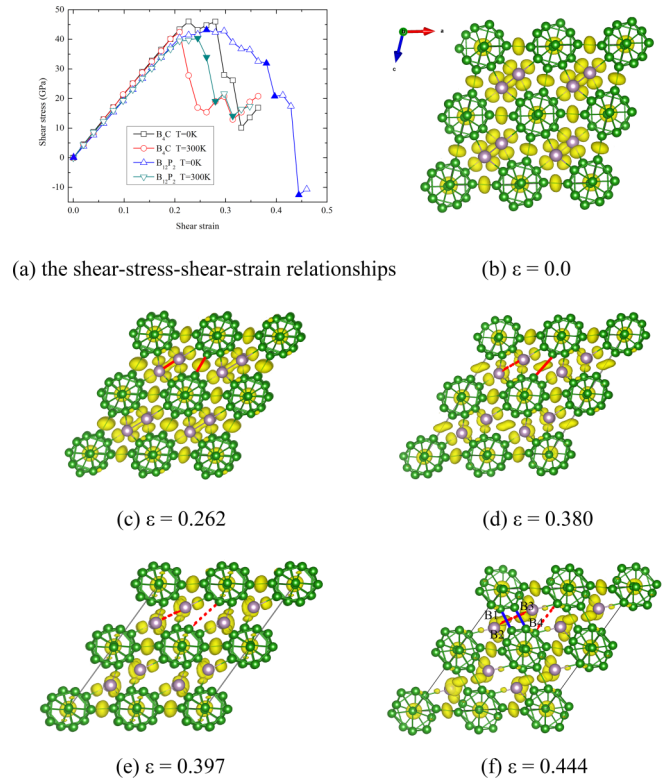
(d) ε = 0.380

(e) ε = 0.397

(f) ε = 0.444

FIG. 9. The shear-stress-shear-strain relationships, calculated isosurfaces (at 0.85) of the electron localization function (ELF) and the structural evolution of $B_{12}P_2$ shearing along the $(001)/[100]$ slip system at $T = 0$ K. (a) The shear-stress-shear-strain relationships. (b) The initial structure. (c) The structure at $\varepsilon = 0.262$, where the P-P bond and icosahedral B-B bond are stretched. (d) The structure at $\varepsilon = 0.380$, where the P-P bond is broken. (e) The structure at $\varepsilon = 0.397$, where the icosahedral B-B bond is broken. (f) The structure at $\varepsilon = 0.444$, where new icosahedral B1-B2 and B3-B4 bonds are formed. The boron and phosphorus atoms are represented by the green and purple balls, respectively.

the structure changes of $B_{12}P_2$ shearing along the $(001)/[100]$ slip system, Figs. 9(b)–9(f) and 10(a)–10(d) show the structures and isoelectron surface (at 0.85) from ELF analysis at various critical strains at $T = 0$ and 300 K, respectively. Figure 9(b) shows the intact structure where ELF indicates the P-P single bond formed in the chain. As the shear strain increases to $\varepsilon = 0.262$, the P-P bond stretches from 2.25 to 2.39 Å, while the B-B bond between icosahedra stretches from 1.74 to 2.04 Å. However, they are not broken [Fig. 9(c)], leading to the monotonic increase in shear stress until reaching its maximum value of 43.20 GPa, as shown in Fig. 9(a). With further shear to $\varepsilon = 0.380$, the P-P bond is broken [Fig. 9(d)], which leads to a lone pair on each P atom. The icosahedral B-B bond increases to 2.55 Å without breaking. Then at $\varepsilon = 0.397$, the shear stress dramatically drops to 20.78 GPa, which arises from the breaking of the icosahedral B-B bond, as shown in Fig. 9(e). As the shear strain increases continuously to $\varepsilon = 0.444$, new B1-B2 and B3-B4 bonds are formed between icosahedra [Fig. 9(f)], leading to structural changes, thereby causing the shear stress to drop to a negative value of −12.54 GPa.

(a) $\varepsilon = 0.245$ (b) $\varepsilon = 0.262$

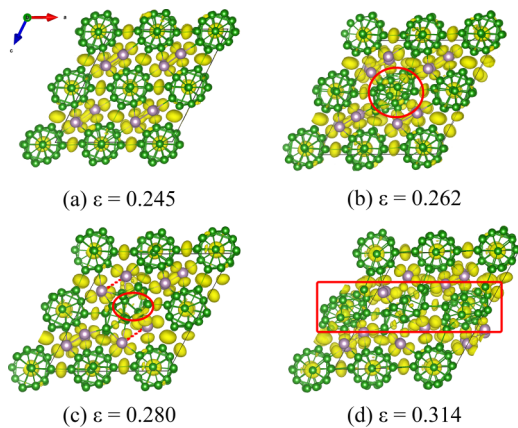(c) $\varepsilon = 0.280$ (d) $\varepsilon = 0.314$

FIG. 10. Calculated isosurfaces (at 0.85) of the electron localization function (ELF) and the structural evolution of $B_{12}P_2$ shearing along the (001)/[100] slip system at $T = 300$ K. (a) The structure at $\varepsilon = 0.245$, where $B_{12}P_2$ deforms elastically. (b) The structure at $\varepsilon = 0.262$, where one of the icosahedra is deconstructed. (c) The structure at $\varepsilon = 0.280$, where the P-P bonds near the deconstructed icosahedron are broken. (d) The structure at $\varepsilon = 0.314$, where one layer of the icosahedra is disintegrated. The boron and phosphorus atoms are represented by the green and purple balls, respectively.

The detailed deformation processes of $B_{12}P_2$ shearing along the (001)/[100] slip system at $T = 300$ K are shown in Figs. 10(a)–10(d). As the shear strain increases to $\varepsilon = 0.245$, the $B_{12}P_2$ structure is uniformly resistant to the elastic deformation, leading to the maximum shear stress to 40.38 GPa. No bond breaks nor forms, as shown in Fig. 10(a). With further shear to $\varepsilon = 0.262$, one of the icosahedra is disintegrated [Fig. 10(b)], causing a sudden drop in shear stress. As the shear strain increases to $\varepsilon = 0.280$, the P-P chains near the deconstructed icosahedron are broken, as displayed in Fig. 10(c), leading to a significant drop in shear stress to 19.06 GPa again. Finally, as the shear strain further increases continuously to $\varepsilon = 0.341$, one layer of B_{12} icosahedral clusters is disintegrated [Fig. 10(d)], thereby giving rise to a significant drop in shear stress to 14.09 GPa. The failure process suggests the local structural failure of $B_{12}P_2$ at finite temperature, thereby causing the lower stress barrier.

Next, we examine the shear deformation of $B_{12}P_2$ along the (111)/[11$\bar{2}$] slip system, where the 2-atom P-P chains are perpendicular to the slip direction, as shown in Fig. S3(c) of the Supplemental Material [40]. Figure 11(a) displays the shear-stress-shear-strain relationships of $B_{12}P_2$ at both $T = 0$ and 300 K. The critical shear stress for $B_{12}P_2$ at $T = 300$ K is 40.57 GPa, which is slightly lower than that at $T = 0$ K (40.97 GPa), implying a lower stress barrier of $B_{12}P_2$ at finite temperature. The detailed deformation processes of $B_{12}P_2$ shearing along the (111)/[11$\bar{2}$] slip system at $T = 0$ K are displayed in Figs. 11(b)–11(f) to illustrate the failure mechanism. Figure 11(b) shows the intact structure. As the shear strain increases to $\varepsilon = 0.322$, the P-P bond is stretched from 2.25 to 2.41 Å, and the B-B bond between icosahedra is stretched from 1.74 to 2.68 Å. The ELF analysis shows that, although the P-P and B-B bonds become weaker significantly, they still exist in the process, leading to the maximum shear stress of 40.79 GPa, as shown in Fig. 11(c). With further shear to

(a) the shear-stress-shear-strain relationships   (b) $\varepsilon = 0.0$

(c) $\varepsilon = 0.322$ (d) $\varepsilon = 0.369$

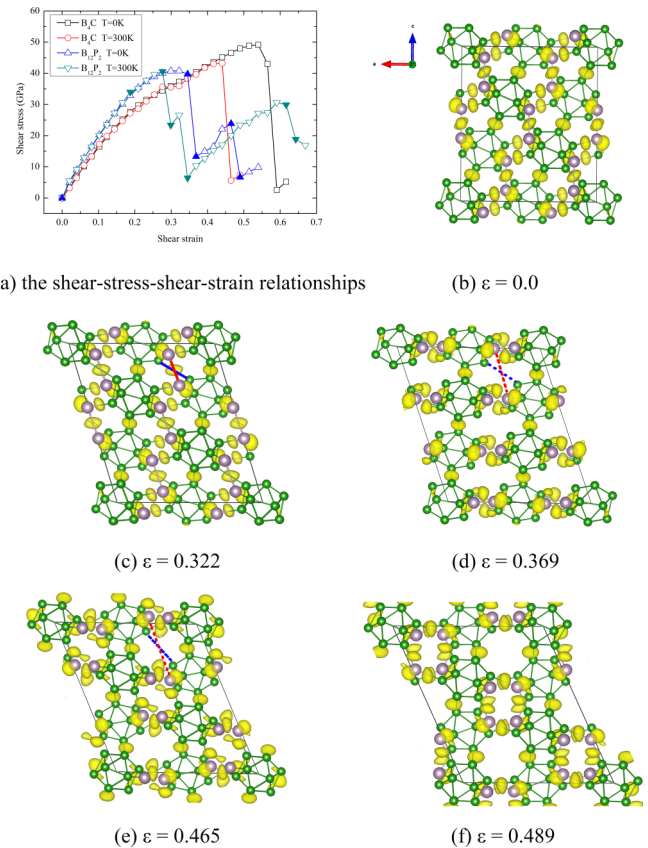(e) $\varepsilon = 0.465$ (f) $\varepsilon = 0.489$

FIG. 11. The shear-stress-shear-strain relationships, calculated isosurfaces (at 0.85) of the electron localization function (ELF) and the structural evolution of $B_{12}P_2$ shearing along the (111)/[11$\bar{2}$] slip system at $T = 0$ K. (a) The shear-stress-shear-strain relationships. (b) The initial structure. (c) The structure at $\varepsilon = 0.322$, where the P-P bond and icosahedral B-B bond are stretched. (d) The structure at $\varepsilon = 0.369$, where the P-P bond and icosahedral B-B bond are broken. (e) The structure at $\varepsilon = 0.465$, where the lattice is rotated. (f) The structure at $\varepsilon = 0.489$, where a new n-$B_{12}P_2$ structure is formed, indicating the structural transition. The boron and phosphorus atoms are represented by the green and purple balls, respectively.

$\varepsilon = 0.369$, both the P-P bond and icosahedral B-B bond are broken [Fig. 11(d)], resulting in a significant drop in shear stress to 13.33 GPa. Then continuous shear to $\varepsilon = 0.465$ leads to the lattice rotation, causing the monotonically increase in shear stress to 43.86 GPa, as displayed in Fig. 11(e). This suggests that the 2-atom P-P chain enables the icosahedra to accommodate additional shear by rotating instead of breaking bonds. Finally, at $\varepsilon = 0.369$, a new $B_{12}P_2$ structure, denoted as the n-$B_{12}P_2$ structure, is formed [Fig. 11(f)], leading to the structural transition, so that the shear stress drops dramatically to 6.69 GPa. This failure process indicates that the structural failure of $B_{12}P_2$ arises from the structural transition instead of amorphization.

Concerning the n-$B_{12}P_2$ structure, its crystal symmetry is orthorhombic with the *CCCM* space group, as shown in Fig. S5 of the Supplemental Material [40]. The optimized lattice parameters of the n-$B_{12}P_2$ structure are $a = 8.054$ Å, $b = 10.446$ Å, and $c = 6.137$ Å, leading to a density of 2.46 g/cm^3. The n-$B_{12}P_2$ structure is 2.46 eV/unit cell

higher in energy than $B_{12}P_2$ based on QM calculations. To determine the stability of the n-$B_{12}P_2$ structure, we computed the enthalpy of formation with respect to the stable forms of boron (α-B_{12}) and phosphorus (P_{42}). The calculated enthalpy of formation for the n-$B_{12}P_2$ structure is -0.614 eV per atom, suggesting the probability of synthesizing this new predicted material. To further validate that the n-$B_{12}P_2$ structure is stable at finite temperature, we performed AIMD simulations on the n-$B_{12}P_2$ structure at room temperature. The results show that n-$B_{12}P_2$ is not decomposed after 3 ps of the MD run, suggesting it is intrinsically metastable at finite temperature. Then to examine the mechanical stability of the n-$B_{12}P_2$ structure, we used QM to predict its elastic constants and elastic modulus and compared with that of $B_{12}P_2$. The calculated elastic constants and elastic modulus of the $B_{12}P_2$ and n-$B_{12}P_2$ structures are listed in Tables S1 and S2 of the Supplemental Material [40], respectively. As shown in Table S1 of the Supplemental Material [40], the calculated elastic constants of $B_{12}P_2$ and n-$B_{12}P_2$ structures satisfy the Born stability criteria simultaneously [60] (see Eq. (S1) of the Supplemental Material [40]), indicating that they are mechanically stable. The bulk modulus (B) and shear modulus (G) are predicted by using Voigt-Reuss-Hill averaging [61]. We find B = 163.9 GPa, G = 139.4 GPa for the n-$B_{12}P_2$ structure, which is 18.1% and 27.2% lower than B and G for the $B_{12}P_2$ structure (B = 200.1 GPa, G = 191.6 GPa), respectively. In general, the strength of materials is often judged by indentation hardness, which measures the resistance of materials to deformation at a constant compression load. Thus, our calculated Vickers hardness (H_v) based on G/B [62] for the n-$B_{12}P_2$ structure is $H_v = 26.7$ GPa, which is 29.9% lower than that of $B_{12}P_2$ ($H_v = 38.1$ GPa).

Figures 12(a)–12(f) show the detailed deformation processes of $B_{12}P_2$ shearing along the $(111)/[11\bar{2}]$ slip system at $T = 300$ K. As the shear strain increases to $\varepsilon = 0.209$, the $B_{12}P_2$ system deforms elastically where the P-P bond and icosahedral B-B bond are stretched yet not breaking, as shown in Fig. 12(a). With further shear to $\varepsilon = 0.276$, the ELF analysis shows that the B-B bond between icosahedra becomes weaker significantly [Fig. 12(b)]. Then the shear stress dramatically drops from the maximum value of 40.57 to 23.39 GPa at $\varepsilon = 0.299$, arising from the breaking of the P1-P2 and B1-B2 bonds [Fig. 12(c)]. While in the process, all P-P bonds and icosahedral B-B bonds are not broken except for the P1-P2 and B1-B2 bonds. As the shear stress increases to $\varepsilon = 0.345$, in addition to the P1-P2 and B1-B2 bonds, the P3-P4 and B3-B4 bonds are also deconstructed, resulting in the second significant stress drop to 6.44 GPa, as shown in Fig. 12(d). Figure 12(e) displays the structure before the third significant stress drop at $\varepsilon = 0.616$, where all P-P bonds and icosahedral B-B bonds still exist except for the P1-P2, P3-P3, B1-B2, and B3-B4 bonds. As the shear stress further increases to $\varepsilon = 0.642$, all P-P bonds and the stretched icosahedral B-B bonds are broken [Fig. 12(f)], leading to structural changes, thereby causing the shear stress to drop significantly to 18.85 GPa. However, the icosahedra in $B_{12}P_2$ are still intact without fracturing, which leads to improved ductility.

In addition, our previous QM studies showed that R-B_6O shearing along the $(011)/[2\bar{1}\bar{1}]$ slip system has the lowest ideal shear stress, resulting in icosahedra disintegration that

(a) $\varepsilon = 0.209$ (b) $\varepsilon = 0.276$

(c) $\varepsilon = 0.299$ (d) $\varepsilon = 0.345$

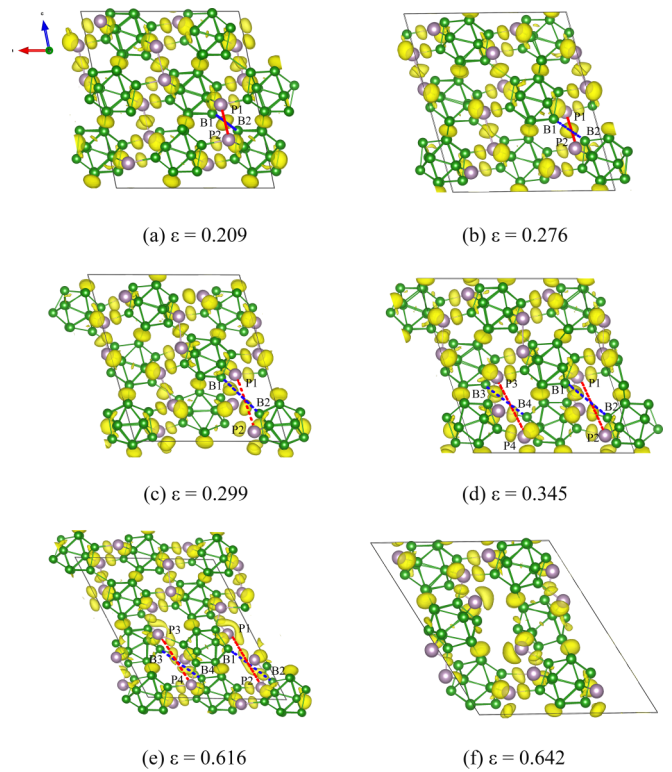(e) $\varepsilon = 0.616$ (f) $\varepsilon = 0.642$

FIG. 12. Calculated isosurfaces (at 0.85) of the electron localization function (ELF) and the structural evolution of $B_{12}P_2$ shearing along the $(111)/[11\bar{2}]$ slip system at $T = 300$ K. (a) The structure at $\varepsilon = 0.209$, where the P-P bond and icosahedral B-B bond are stretched. (b) The structure at $\varepsilon = 0.279$, where the icosahedral B-B bond becomes weaker significantly. (c) The structure at $\varepsilon = 0.299$, where the P1-P2 bond and icosahedral B1-B2 bond are broken. (d) The structure at $\varepsilon = 0.345$, where P1-P2 and P3-P4 bonds and icosahedral B1-B2 and B3-B4 bonds are broken. (e) The structure at $\varepsilon = 0.616$ before the second shear stress drop. (f) The structure at $\varepsilon = 0.642$, where all P-P bonds and the stretched icosahedral B-B bonds are broken, leading to the structural changes. The boron and phosphorus atoms are represented by the green and purple balls, respectively.

leads to the formation of an amorphous shear band along the (011) plane [63]. Since $B_{12}P_2$ has a similar crystal structure to that of R-B_6O, we also examined the deformation process of $B_{12}P_2$ shearing along the $(011)/[2\bar{1}\bar{1}]$ slip system at $T = 0$ and 300 K, as shown in Figs. S6 and S7 of the Supplemental Material, respectively [40]. The failure process suggests that the deconstruction of icosahedra does not occur in $B_{12}P_2$, and the main deformation mechanism is the icosahedral slipping caused by the breaking of chains.

The deformation mode of $B_{12}P_2$ suggests that, since the strength of the icosahedron in $B_{12}P_2$ is stronger than that of the chain bond, the accumulated stress can be released by icosahedral slipping without fracturing icosahedra, which is achieved by breaking the chain. This indicates that the dislocation and deformation twinning may be formed in $B_{12}P_2$ at high-stress conditions, leading to improved ductility. Thus, modifying the chain structure from the 3-atom chain to a 2-atom chain and making sure the strength of the 2-atom chain is less than that

of the icosahedron can be a promising way to improve the ductility of boron carbide.

D. Discussion

In this paper, we focus on the shear deformation of B_4C along two important slip systems which are closely related to the amorphization of B_4C and then propose several strategies to suppress the amorphization. Since amorphization is the onset of structural failure in B_4C, suppressing the amorphization can effectively improve the ability of B_4C to resist abnormal brittle failure and may improve the ductility. The ductility of B_4C may also be associated with other activated slip systems under specific loading conditions as well as superimposed pressures and high temperatures in shock loading and hypervelocity impact. Future experimental or theoretical studies may provide more insights on the improved ductility of $B_{13}C_2$ and $B_{12}P_2$ suggested from this paper.

In this paper, we demonstrated that replacing the $B_{11}C^P$ icosahedron in B_4C with the B_{12} icosahedron to form boron-rich boron carbide ($B_{13}C_2$) may modify the deformation mechanism from full destruction where all icosahedra are disintegrated to local destroy, resulting in improved ductility. Altering the 3-atom chain with a 2-atom chain is another strategy to improve ductility because the accumulated stress can be released by icosahedral slipping without fracturing the icosahedra.

Defects, such as twinning and grain boundaries, are ubiquitous in B_4C. However, the previous experiments on the amorphization of B_4C showed that the amorphous band is not close to the planar defects, nanotwins [9]. This paper suggests that the local amorphization of B_4C occurs if the local stress is higher than the critical shear stress. In addition, the transgranular fracture in B_4C is an important fracture mode in polycrystalline boron carbide with sharp and clean grain boundaries, and the fracture is closely related to the amorphization of B_4C. Our design strategy in this paper should also be helpful to suppress the amorphization within the grain. Thus, although the role of defects is not considered in this paper, it is also important and meaningful to understand the design strategies for improving the ductility of B_4C.

IV. CONCLUSIONS

In summary, we performed AIMD simulations to investigate the finite-temperature deformation behaviors of B_4C shearing along two plausible slip systems $(001)/[100]$ and

$(111)/[11\bar{2}]$ for explaining the effect of temperature on its deformation mechanism. Under pure shear deformation along the $(001)/[100]$ slip system, the failure mechanism of B_4C involves the deconstruction of icosahedra caused by the interaction of the C-B-C chains with the icosahedral clusters. Under pure shear deformation along the $(111)/[11\bar{2}]$ slip system, the brittle failure of B_4C arises from the destruction of 3-atom chains without disintegrating icosahedra. At the finite temperature $T = 300\,\mathrm{K}$, the stress threshold of B_4C is lower than that at $T = 0\,\mathrm{K}$, which arises from the different failure mechanisms. Particularly, the icosahedra in B_4C are gradually destroyed at finite temperature instead of fully disintegrated simultaneously at $T = 0\,\mathrm{K}$, leading to local amorphous shear band formation, thereby giving rise to a lower stress barrier of amorphization in B_4C.

We then examined the deformation process of $B_{13}C_2$ and $B_{12}P_2$ shearing along $(001)/[100]$ and $(111)/[11\bar{2}]$ slip systems to illustrate the design strategies toward improved ductility of B_4C. The $B_{13}C_2$ exhibits local structural failure under shear deformation instead of full destruction of the whole simulation supercell, which arises from the modified icosahedral interaction, thereby mitigating the amorphous shear band formation and then improving ductility. The major deformation mechanism for $B_{12}P_2$ is the icosahedral slipping, which is achieved by the broken chains while avoiding the icosahedral fracture that leads to brittle failure, because the strength of the 2-atom P-P chain is less than that of the icosahedron. This may suppress the amorphization and then improve ductility.

Therefore, we proposed two strategies to improve the ductility of boron carbide:

(1) variations in the stoichiometry of boron carbide, particularly boron enrichment, and

(2) replacing the 3-atom CBC chain with a 2-atom chain and meanwhile decreasing the strength of the chain to make it lower than that of the icosahedron.

Finally, we identified a new $B_{12}P_2$ phase, denoted as n-$B_{12}P_2$, when we shear the $B_{12}P_2$ along the $(111)/[11\bar{2}]$ slip system. This n-$B_{12}P_2$ phase is metastable at finite temperature and exhibits less hardness than $B_{12}P_2$.

ACKNOWLEDGMENTS

---

[1] V. Domnich, S. Reynaud, R. A. Haber, and M. Chhowalla, Boron carbide: Structure, properties, and stability under stress, J. Am. Ceram. Soc. **94**, 3605 (2011).

[2] L. Farbaniec, J. D. Hogan, and K. T. Ramesh, Micromechanisms associated with the dynamic compressive failure of hot-pressed boron carbide, Scr. Mater. **106**, 52 (2015).

[3] F. Thévenot, Boron carbide—a comprehensive review, J. Eur. Ceram. Soc. **6**, 205 (1990).

[4] T. J. Vogler, W. D. Reinhart, and L. C. Chhabildas, Dynamic behavior of boron carbide, J. Appl. Phys. **95**, 4173 (2004).

[5] L. Farbaniec, J. D. Hogan, K. Y. Xie, M. Shaeffer, K. J. Hemker, and K. T. Ramesh, Damage evolution of hot-pressed boron carbide under confined dynamic compression, Int. J. Impact Eng. **99**, 75 (2017).

[6] Y. Zhang, T. Mashimo, Y. Uemura, M. Uchino, M. Kodama, K. Shibata, K. Fukuoka, M. Kikuchi, T. Kobayashi, and T. Sekine,

Shock compression behaviors of boron carbide (B_4C), J. Appl. Phys. **100**, 113536 (2006).

[7] M. Chen, J. W. McCauley, and K. J. Hemker, Shock-induced localized amorphization in boron carbide, Science **299**, 1563 (2003).

[8] D. Ge, V. Domnich, T. Juliano, E. A. Stach, and Y. Gogotsi, Structural damage in boron carbide under contact loading, Acta Mater. **52**, 3921 (2004).

[9] K. M. Reddy, P. Liu, A. Hirata, T. Fujita, and M. W. Chen, Atomic structure of amorphous shear bands in boron carbide, Nat. Commun. **4**, 2483 (2013).

[10] M. Chen and J. W. McCauley, Mechanical scratching induced phase transitions and reactions of boron carbide, J. Appl. Phys. **100**, 123517 (2006).

[11] R. S. Kumar, D. Dandekar, A. Leithe-Jasper, T. Tanaka, Y. Xiao, P. Chow, M. F. Nicol, and A. L. Cornelius, Inelastic x-ray scattering experiments on B_4C under high static pressures, Diam. Relat. Mater. **19**, 530 (2010).

[12] S. Zhao, B. Kad, B. A. Remington, J. C. Lasalvia, C. E. Wehrenberg, and K. D. Behler, Directional amorphization of boron carbide subjected to laser shock compression, Proc. Natl. Acad. Sci. USA **113**, 12088 (2016).

[13] D. Gosset, S. Miro, S. Doriot, G. Victor, and V. Motte, Evidence of amorphisation of B_4C boron carbide under slow, heavy ion irradiation, Nucl. Instrum. Methods Phys. Res. B **365**, 300 (2015).

[14] X. Q. Yan, Z. Tang, L. Zhang, J. J. Guo, C. Q. Jin, Y. Zhang, T. Goto, J. W. McCauley, and M. W. Chen, Depressurization Amorphization of Single-Crystal Boron Carbide, Phys. Rev. Lett. **102**, 075505 (2009).

[15] Q. An and W. A. Goddard III, Atomistic Origin of Brittle Failure of Boron Carbide from Large-Scale Reactive Dynamics Simulations: Suggestions toward Improved Ductility, Phys. Rev. Lett. **115**, 105501 (2015).

[16] J. Li, S. Xu, J. Zhang, L. Liu, Q. Liu, W. She, and Z. Fu, *Ab initio* study on the anisotropy of mechanical behavior and deformation mechanism for boron carbide, Chin. Phys. B **26**, 047101 (2017).

[17] X. Q. Yan, W. J. Li, T. Goto, and M. W. Chen, Raman spectroscopy of pressure-induced amorphous boron carbide, Appl. Phys. Lett. **88**, 131905 (2006).

[18] P. Korotaev, P. Pokatashkin, and A. Yanilkin, The role of non-hydrostatic stresses in phase transitions in boron carbide, Comput. Mater. Sci. **121**, 106 (2016).

[19] Q. An, W. A. Goddard III, and T. Cheng, Atomistic Explanation of Shear-Induced Amorphous Band Formation in Boron Carbide, Phys. Rev. Lett. **113**, 095501 (2014).

[20] K. Y. Xie, Q. An, T. Sato, A. J. Breen, S. P. Ringer, W. A. Goddard III, J. M. Cairney, and K. J. Hemker, Breaking the icosahedra in boron carbide, Proc. Natl. Acad. Sci. USA **113**, 12012 (2016).

[21] K. M. Reddy, D. Guo, S. Song, C. Cheng, J. Han, X. Wang, Q. An, and M. Chen, Dislocation-mediated shear amorphization in boron carbide, Sci. Adv. **7**, eabc6714 (2021).

[22] T. Fujita, P. Guan, K. Madhav Reddy, A. Hirata, J. Guo, and M. Chen, Asymmetric Twins in Rhombohedral Boron Carbide, Appl. Phys. Lett. **104**, 021907 (2014).

[23] K. Y. Xie, Q. An, M. F. Toksoy, J. W. McCauley, R. A. Haber, W. A. Goddard III, and K. J. Hemker, Atomic-Level Under-

standing of "Asymmetric Twins" in Boron Carbide, Phys. Rev. Lett. **115**, 175501 (2015).

[24] D. E. Grady, Adiabatic shear failure in brittle solids, Int. J. Impact Eng. **38**, 661 (2011).

[25] J. D. Clayton, Towards a nonlinear elastic representation of finite compression and instability of boron carbide ceramic, Philos. Mag. **92**, 2860 (2012).

[26] A. Awasthi and G. Subhash, Deformation behavior and amorphization in icosahedral boron-rich ceramics, Prog. Mater. Sci. **112**, 100664 (2020).

[27] M. Devries, G. Subhash, and A. Awasthi, Shocked ceramics melt: an atomistic analysis of thermodynamic behavior of boron carbide, Phys. Rev. B **101**, 144107 (2020).

[28] B. Tang, Y. He, W. A. Goddard III, and Q. An, First principles predicting enhanced ductility of boride carbide through magnesium microalloying, J. Am. Chem. Soc. **102**, 5514 (2019).

[29] V. Adasch, M. Schroeder, D. Kotzott, T. Ludwig, N. Vojteer, and H. Hillebrecht, Synthesis, crystal structure, and properties of $Mg_xB_{50}C_8$ or $Mg_x(B_{12})_4(CBC)_2(C_2)_2$ ($x = 2.4$-4), J. Am. Chem. Soc. **132**, 13723 (2010).

[30] H. Hillebrecht, N. Vojteer, V. Sagawe, K. Hofmann, and B. Albert, Synthesis and characterization of Li-containing boron carbide r-$Li_{\sim 1}B_{13}C_2$, Z. Anorg. Allg. Chem. **645**, 362 (2019).

[31] Y. He, Y. Shen, B. Tang, and Q. An, Strengthening boron carbide through lithium dopant, J. Am. Ceram. Soc. **103**, 2012 (2020).

[32] J. E. Proctor, V. Bhakhri, R. Hao, T. J. Prior, T. Scheler, E. Gregoryanz, M. Chhowalla, and F. Giulani, Stabilization of boron carbide via silicon doping, J. Phys. Condens. Matter **27**, 015401 (2015).

[33] Q. An and W. A. Goddard III, Microalloying boron carbide with silicon to achieve dramatically improved ductility, J. Phys. Chem. Lett. **5**, 4169 (2014).

[34] Q. An and W. A. Goddard III, Improved ductility of B_{12} icosahedra-based superhard materials through icosahedral slip, J. Phys. Chem. C **121**, 11831 (2017).

[35] B. Tang, Q. An, and W. A. Goddard III, Improved ductility of boron carbide by microalloying with boron suboxide, J. Phys. Chem. C **119**, 24649 (2015).

[36] Y. Shen, G. Li, and Q. An, Enhanced fracture toughness of boron carbide from microalloying and nanotwinning, Scr. Mater. **162**, 306 (2019).

[37] Y. He, Y. Shen, B. Tang, and Q. An, Enhanced strength and ductility of superhard boron carbide through injecting electrons, J. Eur. Ceram. Soc. **40**, 4428 (2020).

[38] B. Morosin, G. H. Kwei, A. C. Lawson, T. L. Aselage, and D. Emin, Neutron powder diffraction refinement of boron carbides nature of intericosahedral chains, J. Alloys Compd. **226**, 121 (1995).

[39] R. Lazzari, N. Vast, J. M. Besson, S. Baroni, and A. D. Corso, Atomic Structure and Vibrational Properties of Icosahedral B_4C Boron Carbide, Phys. Rev. Lett. **83**, 3230 (1999).

[40] See Supplemental Material at http://link.aps.org/supplemental/ 10.1103/PhysRevB.104.134105 for additional information pertaining to the crystal structures and ideal shear simulation models of, $B_{13}C_2$, and $B_{12}P_2$, the RDF for B_4C shearing along (001)/[100], the crystal structure of n-$B_{12}P_2$, the shear-stress-shear-strain relationships, and the structural evolution of $B_{12}P_2$ shearing along (011)/[211] slip system at $T = 0$ and 300 K, as

well as the predicted elastic constants and elastic properties for $B_{12}P_2$ and n-$B_{12}P_2$, and the equation of Born stability criteria.

[41] D. E. Taylor, J. W. McCauley, and T. W. Wright, The effects of stoichiometry on the mechanical properties of icosahedral boron carbide under loading, J. Phys. Condens. Matter **24**, 505402 (2012).

[42] D. E. Taylor, Shock compression of boron carbide: a quantum mechanical analysis, J. Am. Ceram. Soc. **98**, 3308 (2015).

[43] A. U. Khan, A. M. Etzold, X. Yang, V. Domnich, K. Y. Xie, C. Hwang, K. D. Behler, M. Chen, Q. An, J. C. LaSalvia, K. J. Hemker, W. A. Goddard III, and R. A. Haber, Locating Si Atoms in Si-Doped Boron Carbide: A route to understand amorphization mitigation mechanism, Acta Mater. **157**, 106 (2018).

[44] Q. Yang, C. Hwang, C. J. Marvel, A. Chauhan, V. Domnich, A. U. Khan, J. C. LaSalvia, M. P. Harmer, K. J. Hemker, and R. A. Haber, Fabrication and characterization of arc melted Si/B Co-doped boron carbide, J. Eur. Ceram. Soc. **39**, 5156 (2019).

[45] Q. An and W. A. Goddard III, Nanotwins soften boron-rich boron carbide ($B_{13}C_2$), Appl. Phys. Lett. **110**, 111902 (2017).

[46] A. Chauhan, M. C. Schaefer, R. A. Haber, and K. J. Hemker, Experimental observations of amorphization in stoichiometric and boron-rich boron carbide, Acta Mater. **181**, 207 (2019).

[47] Q. An and W. A. Goddard III, Ductility in crystalline boron sub-phosphide ($B_{12}P_2$) for large strain indentation, J. Phys. Chem. C **121**, 16644 (2017).

[48] Q. An and W. A. Goddard III, Boron suboxide and boron subphosphide crystals: hard ceramics that shear without brittle failure, Chem. Mater. **27**, 2855 (2015).

[49] Y. Li, Y. H. Zhao, W. Liu, Z. H. Zhang, R. G. Vogt, E. J. Lavernia, and J. M. Schoenung, Deformation twinning in boron carbide particles within nanostructured Al 5083/B_4C metal matrix composites, Philos. Mag. **90**, 783 (2010).

[50] M. Born and V. Fock, Beweis des adiabatensatzes, Z. Phys. **51**, 165 (1928).

[51] G. Kresse and J. Furthmüller, Efficiency of *ab-initio* total energy calculations for metals and semiconductors using a plane-wave basis set, Comput. Mater. Sci. **6**, 15 (1996).

[52] G. Kresse and J. Furthmüller, Efficient iterative schemes for *ab initio* total-energy calculations using a plane-wave basis set, Phys. Rev. B **54**, 11169 (1996).

[53] G. Kresse, From ultrasoft pseudopotentials to the projector augmented-wave method, Phys. Rev. B **59**, 1758 (1999).

[54] J. P. Perdew, K. Burke, and M. Ernzerhof, Generalized Gradient Approximation Made Simple, Phys. Rev. Lett. **77**, 3865 (1996).

[55] P. E. Blöchl, Projector augmented-wave method, Phys. Rev. B **50**, 17953 (1994).

[56] B. Silvi and A. Savin, Classification of chemical-bonds based on topological analysis of electron localization functions, Nature (London) **371**, 683 (1994).

[57] A. D. Becke and K. E. Edgecombe, A simple measure of electron localization in atomic and molecular systems, J. Chem. Phys. **92**, 5397 (1990).

[58] K. Momma and F. Izumi, VESTA 3 for three-dimensional visualization of crystal, volumetric and morphology data, J. Appl. Cryst. **44**, 1272 (2011).

[59] T. Aselage, D. Tallant, and D. Emin, Isotope dependencies of Raman spectra of $B_{12}As_2$, $B_{12}P_2$, $B_{12}O_2$, and $B_{12+x}C_{3-x}$: Bonding of intericosahedral chains, Phys. Rev. B **56**, 3122 (1997).

[60] M. Born, On the stability of crystal lattices. I., Math. Proc. Cambridge Philos. Soc. **36**, 160 (1940).

[61] R. Hill, The elastic behaviour of a crystalline aggregate, Proc. Phys. Soc. Sect. A **65**, 349 (1951).

[62] X. Q. Chen, H. Niu, D. Li, and Y. Li, Modeling hardness of polycrystalline materials and bulk metallic glasses, Intermetallics **19**, 1275 (2011).

[63] Q. An, K. M. Reddy, H. Dong, M. W. Chen, A. R. Oganov, and W. A. Goddard III, Nanotwinned boron suboxide (B_6O): new ground state of B_6O, Nano Lett. **16**, 4236 (2016).